APPLIED SCIENCES AND ENGINEERING

Neurorobotic approaches to emulate human motor control with the integration of artificial synapse

Seonkwon Kim[1]†, Seongchan Kim[2]†, Dong Hae Ho[1], Dong Gue Roe[3], Young Jin Choi[1], Min Je Kim[1], Ui Jin Kim[3], Manh Linh Le[4], Juyoung Kim[4]*, Se Hyun Kim[5]*, Jeong Ho Cho[1]*

Copyright © 2022 The Authors, some rights reserved; exclusive licensee American Association for the Advancement of Science. No claim to original U.S. Government Works. Distributed under a Creative Commons Attribution NonCommercial License 4.0 (CC BY-NC).

The advancement of electronic devices has enabled researchers to successfully emulate human synapses, thereby promoting the development of the research field of artificial synapse integrated soft robots. This paper proposes an artificial reciprocal inhibition system that can successfully emulate the human motor control mechanism through the integration of artificial synapses. The proposed system is composed of artificial synapses, load transistors, voltage/current amplifiers, and a soft actuator to demonstrate the muscle movement. The speed, range, and direction of the soft actuator movement can be precisely controlled via the preset input voltages with different amplitudes, numbers, and signs (positive or negative). The artificial reciprocal inhibition system can impart lifelike motion to soft robots and is a promising tool to enable the successful integration of soft robots or prostheses in a living body.

INTRODUCTION

Living organisms have evolved to exhibit efficient functionalities to adapt to their environments. These inherent traits have inspired researchers to develop innovative biomimetic electronics aimed at integrating living organisms and electronic devices (*1*–*10*). In particular, biomimetic approaches for soft robots have enabled the development of soft prostheses that exhibit continuous and natural deformation with large compliance (*11*–*15*). Owing to these characteristics, such devices can easily adapt to different environments while safely interacting with humans (*16*–*18*). To successfully integrate soft robots with the human body, compatibility with the living body, such as the connection with the living organism at the neuronal level and similarity in the signal transmission of the living body, is substantial (*19*). In this context, it is necessary to understand the human motor system and ensure the appropriate incorporation of electronic devices that operate similar to the human nervous system to enable its emulation.

Recent studies on artificial synapses (ASs) successfully demonstrated the movement of actuators by mimicking human motor neurons (*20*–*29*). Notably, these works focused on the operation of actuators by using the signal transmission characteristics of a single AS. However, to enable the application of such devices as prostheses, a bioinspired circuit that mimics the complex signaling system of humans must be developed. Integration of ASs in the conventional logic circuits (e.g., buffer and inverter gates) would further broaden the horizon of AS applications, which can eventually embrace even the emulation of complex biosignaling. Although AS-integrated logic circuits have been widely studied so far (*28*, *30*–*35*), further in-depth investigations on the actual implementation of biomimetic systems are imperative because of their foreseeable advantages in terms of desirable complexity reductions. Considering that complementary metal-oxide semiconductor (CMOS)–based neuromorphic hardware requires more than 10 devices to emulate one synapse, implementing AS would enable compact and lightweight prosthetics for children and frail adults (*36*–*37*). For instance, when a person performs a voluntary movement of a joint, a pair of muscles (an agonist muscle and an antagonist muscle) work in synchrony to ensure a smooth and continuous movement (i.e., reciprocal inhibition) (*38*–*40*). Descending signals from the brain bifurcate in the spinal cord; one branch innervates the alpha motor neuron to contract an agonist muscle, and the other branch innervates the interneuron, causing the relaxation of an antagonist muscle. This aspect is one of the most ubiquitous physiological mechanisms involved in human and animal motor control and has been thoroughly studied since the early 1900s. The emulation of this motor control mechanism of humans via an AS-based artificial motor control system can likely impart lifelike movement to bioinspired soft robots and prostheses.

In this study, we developed an artificial reciprocal inhibition system, inspired by the human physiological mechanism involved in voluntary movements. The designed system consisted of excitatory/inhibitory synapse circuits (ESC/ISC), voltage/current amplifiers, and a soft actuator to demonstrate the muscle movement. An indium tin oxide (ITO)/indium gallium zinc oxide (IGZO)/organic-inorganic (O-I) hybrid dielectric/aluminum (Al) structure was used for both the AS and load transistor constituting the ESC/ISC. The O-I hybrid dielectric exhibits the electrical properties of a typical dielectric when thermally treated at 180°C, whereas it exhibits retentive properties when treated at 230°C. The ESC and ISC, composed of an AS and a load transistor connected via a voltage distributing circuit, are considered an AS-integrated buffer and inverter logic gate, respectively. These circuits were connected to Ni-Ti shape memory alloy (Ni-Ti SMA) fibers comprising the soft actuator, respectively. These fibers represented the agonist and antagonist muscle fibers of human muscle and implemented the synergistic movement through

---

[1] Department of Chemical and Biomolecular Engineering, Yonsei University, Seoul 03722, Republic of Korea. [2] SKKU Advanced Institute of Nanotechnology (SAINT), Sungkyunkwan University, Suwon 16419, Republic of Korea. [3] School of Electrical and Electronic Engineering, Yonsei University, Seoul 03722, Republic of Korea. [4] Department of Advanced Materials Engineering, Kangwon National University, Samcheok 25931, Republic of Korea. [5] Division of Chemical Engineering, Konkuk University, Seoul 05029, Republic of Korea.

*Corresponding author. Email: juyoungk@kangwon.ac.kr (J.K.); shkim97@konkuk.ac.kr (S.H.K.); jhcho94@yonsei.ac.kr (J.H.C.)

†These authors contributed equally to this work.

the contraction of one side with the simultaneous relaxation of the other side. In the designed system, the speed, range, and direction of the soft actuator movement could be precisely controlled via the preset input voltages with different amplitudes, numbers, and signs (positive or negative). Artificial reciprocal inhibition system was successfully controlled with far less circuit complexity with lower energy consumption than a conventional all-CMOS–based system owing to the pulse-based operation of AS. Successful emulation of the reciprocal inhibition found in the human body is expected to promote research on AS-based soft robotics control.

RESULTS

Figure 1A schematically illustrates the descending motor pathway (corticospinal tract), which modulates voluntary muscle movement. First, the precentral gyrus in the brain transmits nerve signals to initiate the muscle movement. These signals bifurcate in the spinal cord, connected in parallel to the agonist and antagonist muscle. One branch facilitates the excitatory alpha-motoneuron (α-MN), and the other branch facilitates the inhibitory interneuron (Ia-IN), which, in turn, innervates the inhibitory α-MN. Figure 1B shows the biological excitatory synapse pathway with the corresponding designed circuit denoted as the ESC. In the biological pathway, the descending signals directly innervate the excitatory α-MN to contract the agonist muscle. Inspired by this signaling mechanism, the ESC is developed using an AS and a load transistor. Presynaptic voltage (V_{pre}) is applied to the AS to facilitate or depress it to control the output voltage of the ESC (denoted as V_{ES}). The biological inhibition synapse pathway with the corresponding circuit denoted as the ISC is shown in Fig. 1C. Descending signals innervate Ia-IN, which converts the descending signals into inhibitory signals, thereby accommodating the relaxation of the antagonist muscle in coordination with the contraction of the agonist muscle. Inspired by this disynaptic inhibition, the ISC is designed to consist of an AS and a load transistor. V_{pre} is applied to the AS to control the output voltage of the ISC (denoted as V_{IS}).

The circuit diagram for the entire system designed by connecting the ESC and ISC in parallel is shown in Fig. 1D. V_{ES} and V_{IS} generated by applying V_{pre} pulses to the AS of the ESC and ISC, which are connected to the common electrode supplied with the drain voltage (V_D), pass through noninverting voltage amplifiers [operational amplifier (OP AMP)] and current amplifiers [bipolar junction transistor (BJT)] to drive the soft actuator. Figure 1 (E and F) schematically illustrate the sequential signal transmission process. With the application of consecutive positive V_{pre} pulses to the AS, as shown in Fig. 1E, the conductance of the AS ($S_{synapse}$) gradually increases on both the ESC and ISC. Increasing $S_{synapse}$ induces gradual potentiation of V_{ES} and depression of V_{IS}. Last, the soft actuator with two electrodes, connected to V_{ES} and V_{IS}, bends in the direction in which V_{ES} is connected owing to the contraction on the V_{ES} side and relaxation on the V_{IS} side. When consecutive negative V_{pre} pulses are applied, as shown in Fig. 1F, $S_{synapse}$, gradually decreases, which induces the depression of V_{ES} and potentiation of V_{IS}. Consequently, the soft actuator bends in the direction of the contracted V_{IS} side, while the V_{ES} side is relaxed. Overall, actuation enabled by the application of either positive or negative V_{pre} pulses capacitates the bidirectional movement.

Figure 2A shows the schematic of a thin-film transistor fabricated using an O-I hybrid gate dielectric (GPSi), the properties of which

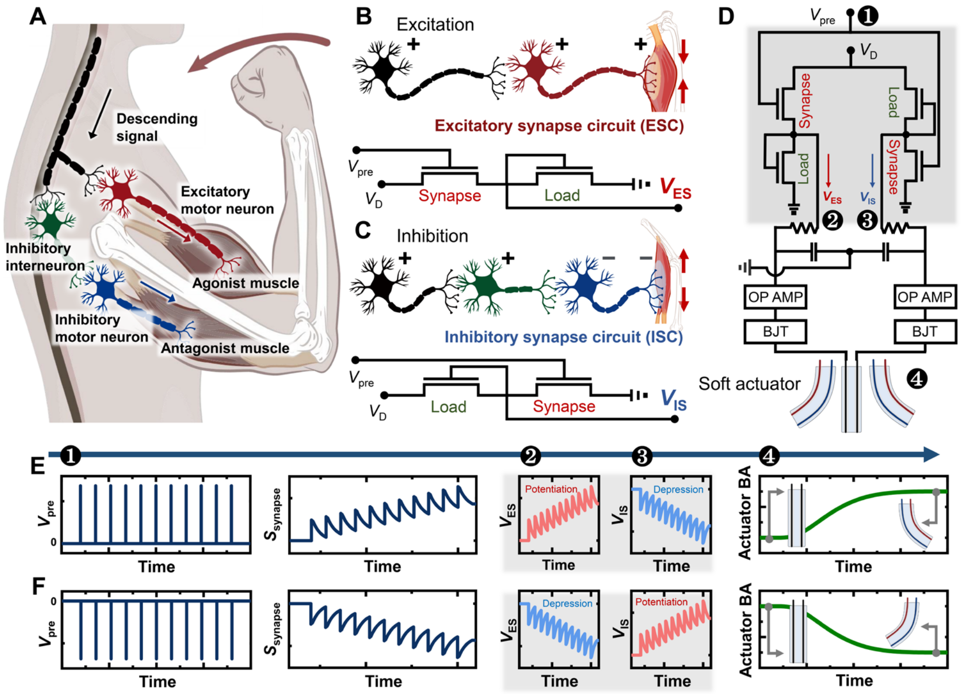
A
Descending signal
Excitatory motor neuron
Inhibitory interneuron
Agonist muscle
Inhibitory motor neuron
Antagonist muscle
B
Excitation
Excitatory synapse circuit (ESC)
V_{pre}
V_D
Synapse
Load
V_{ES}
C
Inhibition
Inhibitory synapse circuit (ISC)
V_{pre}
V_D
Load
Synapse
V_{IS}
D
V_{pre} ❶
V_D
Synapse
Load
Load
Synapse
V_{ES}
V_{IS}
❷
❸
OP AMP
OP AMP
BJT
BJT
Soft actuator
❹
E
❶ ❷ ❸ ❹
V_{pre}
0
Time
$S_{synapse}$
Time
V_{ES}
Potentiation
Time
V_{IS}
Depression
Time
Actuator BA
Time
F
V_{pre}
0
Time
$S_{synapse}$
Time
V_{ES}
Depression
Time
V_{IS}
Potentiation
Time
Actuator BA
Time

Fig. 1. Operation mechanism of artificial reciprocal inhibition system. (**A**) Schematic of biological reciprocal inhibition composed of excitatory motor neuron, inhibitory interneuron, inhibitory motor neuron, agonist muscle, and antagonist muscle. (**B** and **C**) Schematic of biological excitatory/inhibitory synapse pathway with the corresponding circuit. (**D**) Circuit diagram of artificial reciprocal inhibition system. (**E** and **F**) Schematic of the signal transmission process in the artificial reciprocal inhibition system.

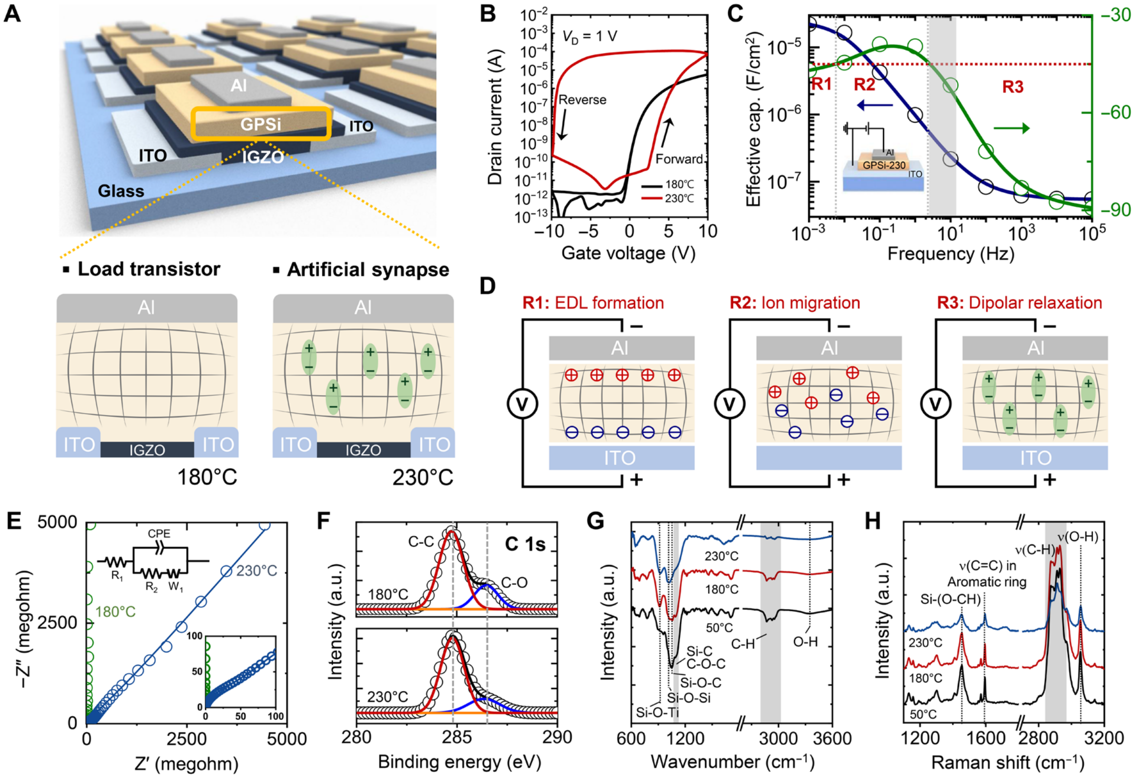

Fig. 2. Chemical analysis of GPSi gate dielectrics. (**A**) Schematic device structure and chemical state of the load transistor and AS. (**B**) Transfer characteristics of GPSi-180 and GPSi-230. (**C**) Capacitance (left) and phase angle (right) properties of GPSi-230 as a function of frequency ranging from 0.001 to 10^5 Hz. (**D**) Schematic of three dielectric polarization mechanisms of the GPSi-230 layer. (**E**) Nyquist plot of GPSi at different annealing temperatures. (**F**) Fourier transform infrared (FTIR) spectra and (**G**) Raman spectra of GPSi annealed at different temperatures. (**H**) X-ray photoelectron spectroscopy (XPS) C 1s spectra of GPSi annealed at different temperatures. a.u., arbitrary units.

vary with the thermal annealing temperature. First, the ITO source and drain electrodes are sputtered onto a glass substrate, followed by the deposition of the IGZO channel. Subsequently, the GPSi dielectric is spin-coated onto the substrate. Last, Al is thermally deposited onto the GPSi film. GPSi sol is prepared using 3-glycidoxy propyl trimethoxysilane, propyltrimethoxysilane, titanium (IV) isopropoxide, and alkoxysilane-functionalized amphiphilic polymer (AFAP) as precursors (fig. S1) (*41*). The sol-gel–derived GPSi films exhibit different behavior under different annealing temperatures owing to the thermal decomposition of the propyl and glycidyl functional groups attached to the corner of the polyhedral oligomeric silsesquioxane (POSS) cage (fig. S2). Figure 2A (bottom) illustrates the chemical states of GPSi at different annealing temperatures. GPSi films annealed at 180°C (GPSi-180) and 230°C (GPSi-230) are used to prepare the load transistor and AS, respectively. Thermal annealing at 230°C induces the bond cleavage of the glycidyl functional groups, resulting in the residue of small molecules with large dipole moments. These small molecules align themselves with the electric field and retain their orientation even after the electric field is removed. Figure 2B shows the transfer characteristics of GPSi-180 and GPSi-230 devices. Although the GPSi-180 device exhibits negligible hysteresis, the GPSi-230 device exhibits large anticlockwise hysteresis of the drain current (I_D) owing to the dipolar relaxation of the residual small molecules. Transfer characteristics of GPSi-based devices under different annealing temperatures and the resulting memory window are shown in fig. S3. The retentive properties of the GPSi-230 device can be observed in the time-dependent I_D measurements (fig. S4).

To investigate the retentive properties of the GPSi-230 film, a metal-insulator-metal structure capacitor test bed is fabricated, as shown in the inset in Fig. 2C. Electrochemical impedance spectroscopy (EIS) measurements of the GPSi-230 film are obtained by applying an AC voltage with a frequency (f) ranging from 10^5 to 0.001 Hz to the capacitor and measuring the complex impedance (Z_{tot}). Figure 2C shows the effective capacitance (C_{eff}) and phase angle (θ) as a function of f, with C_{eff} determined through the Z_{tot} of the capacitor ($C_{eff} = -1/2\pi Z''f$) (*42*). Three regions can be identified on the basis of $\theta = -45°$, which represents whether the capacitive element is dominant ($\theta < -45°$) or the resistive element is dominant ($\theta > -45°$) in the device. As shown in Fig. 2D, the capacitive behavior in R1 ($f < 0.005$ Hz) can be attributed to the formation of an electric double layer at the metal interfaces. The resistive behavior in R2 ($0.005 \text{ Hz} < f < 2.7$ Hz) can be attributed to the ionic relaxation. Last, the transition from R2 to R3 ($f > 2.7$ Hz) indicates the changeover of the ionic contribution to the dipolar contribution (i.e., dipolar relaxation) (*43*). The AS operates in the region of $2.7 \text{ Hz} < f < 10$ Hz (shaded region in Fig. 2C), confirming that the dipolar relaxation governs the retentive behavior of the AS. In contrast, the GPSi-180 exhibits a straight line of $\theta = -90°$ at all frequencies, characteristic of an ideal capacitor (fig. S5). This difference between the GPSi-180 and GPSi-230 films can also be confirmed by the Nyquist plot shown in Fig. 2E (see also fig. S6). Moreover, phase angle change as a function of f under different annealing temperatures is shown in fig. S7.

The retentive behavior of the GPSi-230 film can be characterized by investigating the chemical structure. Therefore, various chemical analyses including the Fourier transform infrared (FTIR) spectroscopy, Raman spectroscopy, x-ray photoelectron spectroscopy (XPS), and thermogravimetric analysis are conducted. Figure 2F shows the FTIR spectra of GPSi annealed at different temperatures. As the hydrolysis/condensation progresses upon thermal annealing, the intensities of the Si-O-C peak at 1056 cm^{-1} and O-H peak at 3400 cm^{-1} decrease; however, the intensities of the peaks at 910 to 960 cm^{-1} and 1029 cm^{-1} corresponding to Si-O-Ti and Si-O-Si, respectively, significantly increase (*44*). In particular, upon annealing at 230°C, the peaks at 2900 to 3000 cm^{-1} (assigned to C-H stretching) and 1080 to 1100 cm^{-1} (corresponding to overlapped peaks of the C-O-C and Si-C bonds) diminish owing to the fragmentation of the propyl and glycidyl functional groups attached to the corners of the POSS cages (*45*–*47*). Existing studies on the thermal treatment of POSS have indicated that the POSS cage can withstand a temperature of up to 450°C (*48*–*52*), although the organic elements start to degrade at 180°C, consistent with the findings of our study. According to the Raman spectra (Fig. 2G), the peaks at 2800 to 3000 cm^{-1}, shaded in gray, which represent C-H stretching, significantly decrease, further supporting presence of bond cleavage of the glycidyl and propyl functional groups. The C-O bond cleavage induced by thermal annealing at 230°C is confirmed by the XPS C 1s spectra of GPSi (Fig. 2H) (*53*). Figure S8 shows the thermal degradation curve of the GPSi; the film begins to lose weight at approximately 200°C and exhibits a weight difference of 4% at 230°C. This result indicates the sublimation of the volatile propyl functional groups, owing to the Si-C bond scission. Furthermore, the contribution of the thermal degradation of AFAP on the retention behavior of GPSi-230 can be excluded, considering the several measurements shown in fig. S9. Overall, the POSS structure gradually develops through the hydrolysis/condensation reaction as the temperature increases; however, the thermal annealing at 230°C induces the bond cleavage of the propyl and glycidyl functional groups in the POSS structure, resulting in the residue of small molecules with large dipole moments.

Figure 3A shows a simplified schematic of the synaptic pathways in the reciprocal inhibition of the agonist-antagonist muscle pair. Disynaptic inhibition of an antagonist muscle along with the excitation of an agonist muscle is activated via a single descending action potential from the central nerve. The synapses constituting this neuromuscular system facilitate the transfer of the action potential from the upper neuron to the lower motor neuron. Inspired by the aforementioned neuromuscular system, an AS with a GPSi-230 gate dielectric is fabricated (Fig. 3B). Various electrical properties of the AS are analyzed. Figure 3C shows the excitatory postsynaptic current (EPSC) of the AS with GPSi-230 as a function of V_{pre} (pulse width, λ_{pre} = 200 ms, 1.5, 2.0, and 2.5 V). The device exhibits the EPSC response as the conductance abruptly increases upon the application of the input spike and gradually decays without converging to the initial value. As the amplitude of the applied voltage increases from 1.5 to 2.5 V, the change in the PSC (ΔPSC) increases from 0.53 to 1.02 nA, 10 s after the spike. The synaptic connection can be controlled via the voltage amplitude, owing to the dependence of the input voltage amplitude on the electric field–induced dipole change of GPSi-230. In contrast, the device with the GPSi-180 gate dielectric exhibits negligible retention properties. This behavior can be confirmed through the inhibitory PSC measurements shown in fig. S10.

Figure 3D shows the long-term potentiation/depression (LTP/D) characteristic of the AS with GPSi-230, measured by applying 100 consecutive potentiation pulses followed by 100 consecutive depression pulses. Each pulse set involves amplitudes of 1.5, 2.0, and 2.5 V for potentiation and −1.0, −1.5, and −2.0 V for depression, with the frequency and width fixed as 2.5 Hz and 200 ms, respectively (frequency dependency of LTP/D characteristic is exhibited in fig. S11). The maximum conductance increases from 5.2 to 10.3 μS as the amplitude of the potentiation pulse increases from 1.5 to 2.5 V. As repeated pulses are applied, the electric field–induced dipole orientation continues to change, and the degree of synaptic connection changes accordingly (also see the LTD behavior shown in fig. S12). Moreover, the PSC response to paired pulses in a short-time interval is investigated, as shown in fig. S13. Figure 3E shows the highly uniform distribution of the dynamic range (G_{max}/G_{min}) of the AS arranged in a 5 × 5 array on a single substrate. The average G_{max}/G_{min} is 2.72 ± 0.19 (× 10^5), and the calculated relative SD is 6.9%. The corresponding distribution and LTP/D results for each device are shown in fig. S14. The operational stability of the AS is investigated by repeatedly applying 100 potentiation pulses, followed by 100 depression pulses for 50 cycles (Fig. 3F). The amplitude of the potentiation and depression voltage are fixed at 1.5 and −1.0 V, respectively. No significant variation can be observed in the shape of the LTP/D curve, from the beginning to the end of the cyclic test (Fig. 3G). Moreover, fig. S15 shows the excellent environmental stability of the AS (also see fig. S16 for temperature-dependent behavior of the AS device). Overall, the AS with GPSi-230 exhibits high uniformity and operational stability, although the retention property of the device is based on the thermal decomposition of the GPSi film.

Inspired by the excitatory and inhibitory synapses in the biological system, we construct AS circuits, ESC and ISC, as shown in Fig. 3H, by integrating the AS with GPSi-230 and load transistor with GPSi-180 (Fig. 2A), respectively. The ESC and ISC are designed on the basis of voltage divider circuits consisting of an AS and a load transistor connected in series. For the ESC, the AS is connected to the drain terminal of the load transistor, whereas the AS is connected to the source terminal of the load transistor for the ISC. The output voltages, denoted as V_{out} (V_{ES} or V_{IS}), are determined as $V_{ES} = V_D\,[S_{load}^{-1}/(S_{load}^{-1} + S_{synapse}^{-1})]$ and $V_{IS} = V_D\,[S_{synapse}^{-1}/(S_{load}^{-1} + S_{synapse}^{-1})]$, where $S_{synapse}$ and S_{load} denote the conductance of the AS and load transistor, respectively. V_{out} responses to V_{pre} are examined by sweeping the V_{pre} from −10 V to 10 V (fig. S17), consistent with the change $S_{synapse}$.

The change in V_{out} is deterministically controlled by varying the number and amplitude of V_{pre} pulses. First, pulse sets with different number of pulses are applied to the V_{pre} terminal to investigate the response of V_{out} to the number of V_{pre} pulses (Fig. 3I). Specifically, potentiation V_{pre} pulses of +2 V are applied 25, 50, 75, and 100 times to the V_{pre} terminal, followed by the application of depression pulses of −2 V with the same number of pulses. Application of the potentiation pulses to the V_{pre} terminal increases the synaptic connection of the AS, leading to an increase in V_{ES} and decrease in V_{IS}. In contrast, the application of depression pulses reduces the synaptic connection and leads to a contrasting result. The resulting maximum V_{ES} and minimum V_{IS} are summarized in Fig. 3J under various number of pulses. As the number of pulses increases from 25 to 100, the maximum V_{ES} increases from 0.53 to 0.81 V and minimum V_{IS} decreases from 0.59 to 0.11 V.

Furthermore, the change in V_{out} is investigated by varying the amplitude of the V_{pre} pulse of each circuit. V_{out} is set as 0.5 V before

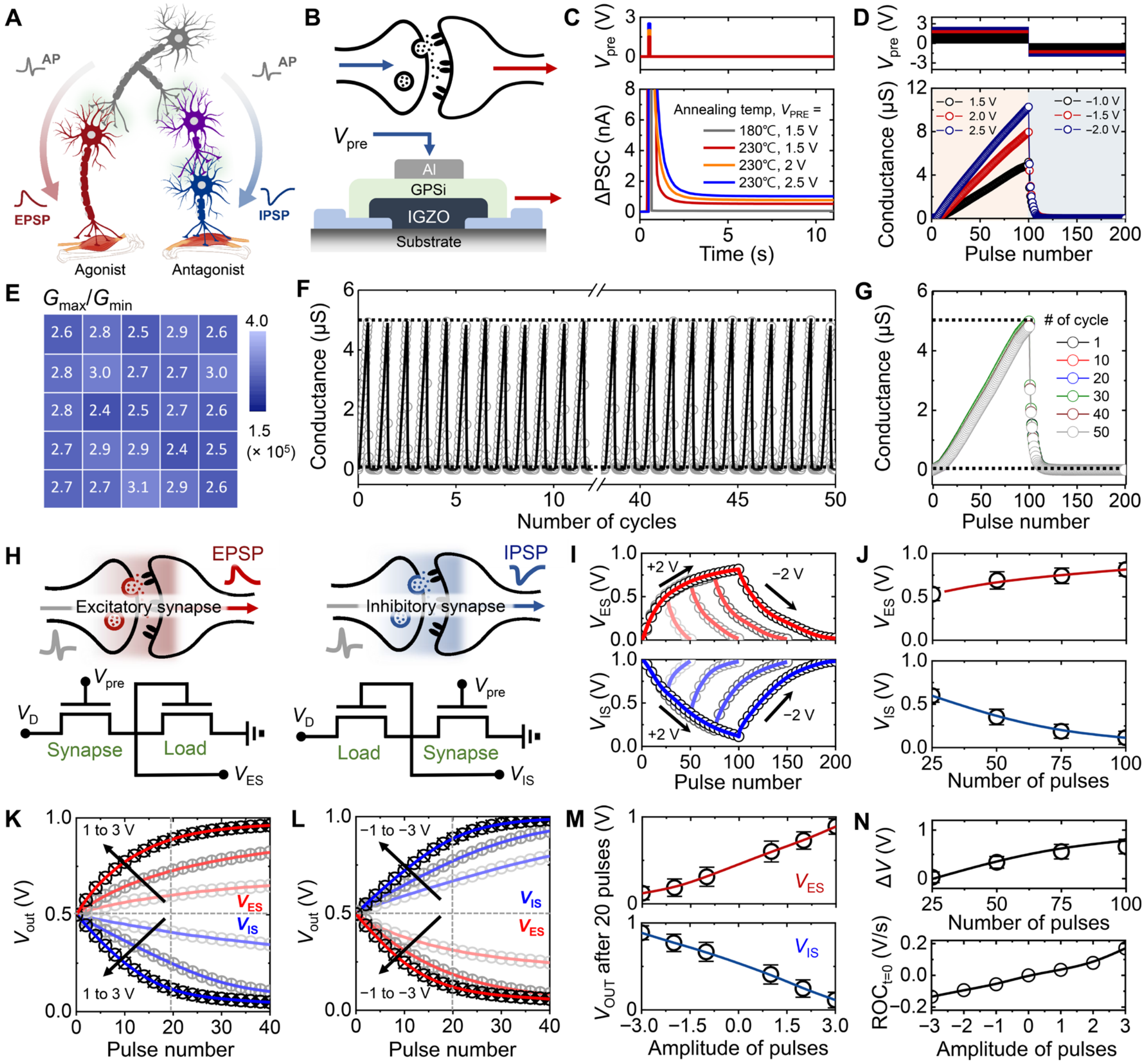

Fig. 3. Electrical properties of ESC and ISC. (**A**) Schematic of biological synaptic pathways in reciprocal inhibition of agonist and antagonist muscle pair. (**B**) Schematic of biological synapse with the corresponding AS. (**C**) Comparison of PSC properties between a load transistor with GPSi-180 and AS with GPSi-230. (**D**) LTP/D characteristic of AS subjected to 100 consecutive potentiation pulses (V_{pre} = 1.5, 2.0, and 2.5 V), followed by 100 consecutive depression pulses (V_{pre} = −1.0, −1.5, and −2.0 V). (**E**) Distribution of G_{max}/G_{min} of the AS arranged in a 5 × 5 array on a single substrate. (**F**) LTP/D characteristics of AS over 50 cycles. (**G**) Cycle-to-cycle variations of LTP/D curve over 50 cycles. (**H**) Schematic of biological excitatory synapse and inhibitory synapse with the constructed corresponding circuits. (**I**) V_{ES} and V_{IS} observed after application of 25, 50, 75, and 100 consecutive potentiation pulses (V_{pre} = 2.0 V), followed by 25, 50, 75, and 100 consecutive depression pulses (V_{pre} = −2.0 V). (**J**) Maximum V_{ES} and minimum V_{IS} after application of 25, 50, 75, and 100 consecutive potentiation pulses. V_{ES} and V_{IS} observed after application of (**K**) +1 to +3 V and (**L**) −1 to −3 V for 40 consecutive pulses. (**M**) V_{ES} and V_{IS} values after application of 20 pulses with varying pulse amplitudes. (**N**) Plots of ΔV as a function of number of pulses (top) and $ROC_{t=0}$ values as a function of amplitude of pulses (bottom).

the measurement (see fig. S18 for the adjustment), and 40 consecutive input pulses of +1 to +3 V (Fig. 3K) and −1 to −3 V (Fig. 3L) are applied. Figure 3M presents the values of V_{ES} and V_{IS} after the application of V_{pre} 20 times with varying amplitudes. Higher values of V_{out} are obtained in the case of V_{pre} pulses with higher amplitudes. Moreover, V_{pre} pulses with higher amplitudes induce a larger change in the synaptic connection of the AS in the same period, resulting in a steeper V_{out} change. Figure S19 shows the rate of change (ROC) of V_{ES} and V_{IS} at $t = 0$ (the derivative of V_{out} by time at $t = 0$) as a function of the V_{pre} amplitude. Figure 3N (top) shows the value of $V_{ES} - V_{IS}$ (denoted as ΔV) after the application of varying number of pulses. ΔV represents the difference in the synaptic connection of the ESC and ISC, which is an essential parameter that induces the deformation of the soft actuator. The findings indicate that the range of soft actuator movements can be precisely controlled through the number of applied V_{pre} pulses. Figure 3N (bottom) shows the ROC of ΔV at $t = 0$ as a function of the pulse amplitude. The findings indicate that the speed of the soft actuator movement can be precisely controlled through the amplitude of the V_{pre} pulses. Overall, the designed system can emulate the range and speed control mechanism of voluntary muscles in the biological system.

Inspired by the reciprocal inhibition of agonist-antagonist pair in the biological system, an artificial reciprocal inhibition system (ARIS) is constructed using the ESC and ISC. Figure 4A shows the circuit

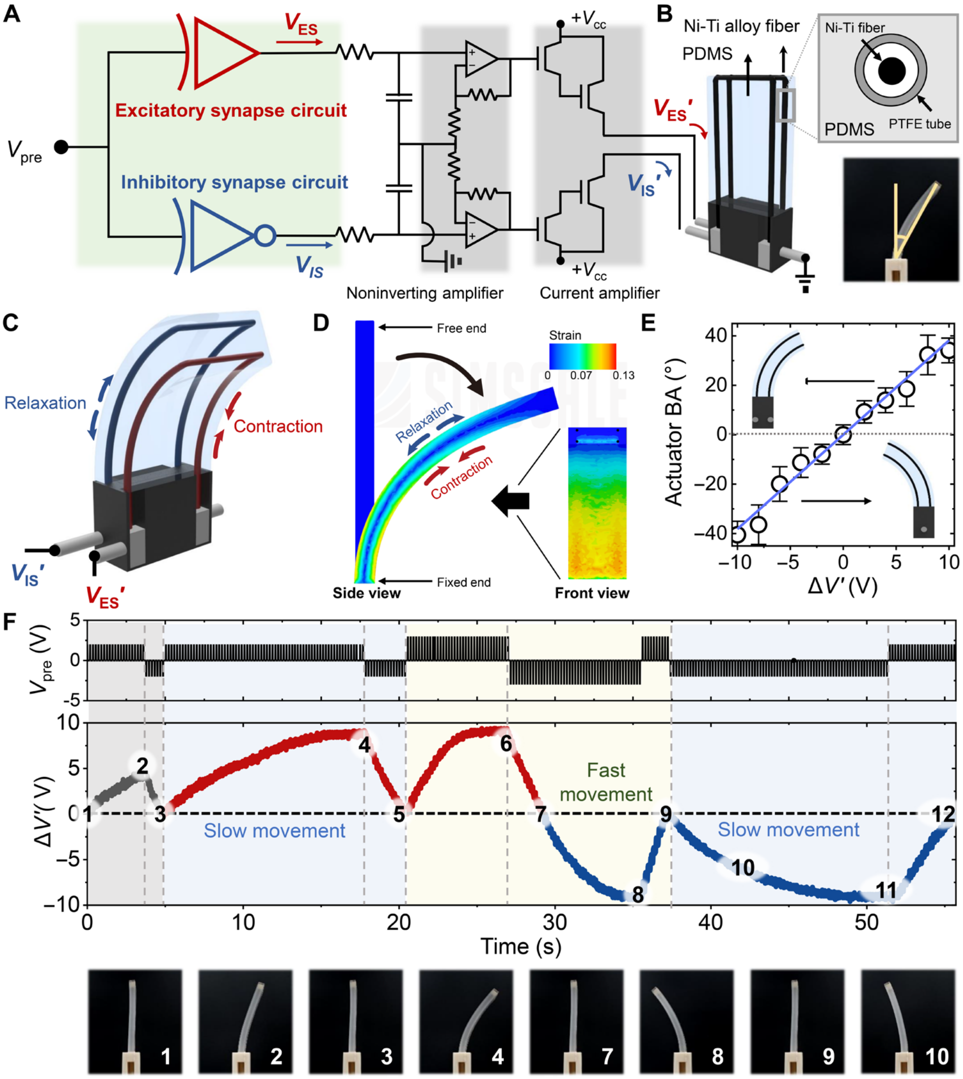

Fig. 4. Artificial reciprocal inhibition system. (**A**) Circuit diagram of artificial reciprocal inhibition system with ESC, ISC, voltage/current amplifiers, and a soft actuator. (**B**) Schematic of the Ni-Ti SMA fiber–embedded soft actuator, along with cross section of the actuator and photograph of the actuator indicating the BA. (**C**) 3D schematic of the bending actuator when subjected to V_{ES}' and V_{IS}' on each fiber. (**D**) Side and front views of the strain distribution based on the simulated results of a bending actuator. (**E**) Actuator BA as a function of $\Delta V'$ with the fitted line. (**F**) Real-time $\Delta V'$ measurement with the corresponding photographic images of the soft actuator. Photo credit: Seonkwon Kim (Department of Chemical and Biomolecular Engineering, Yonsei University).

diagram of the constructed system, which includes the ESC, ISC, RC circuit, noninverting voltage amplifier, current amplifier, and soft actuator. A photograph of the whole system implementation is shown in fig. S20. The ARIS is initiated by applying input pulses to the ESC and ISC connected in parallel, which convert the input pulse (V_{pre}) to V_{ES} and V_{IS}, respectively. To reduce the electrical signal noise, an RC circuit that functions as a low-pass filter is added (fig. S21). Subsequently, the filtered signals pass through the noninverting voltage amplifier and current amplifier and are eventually converted to V_{ES}' and V_{IS}', which drive the soft actuator. The difference in V_{ES}' and V_{IS}' causes the deformation of the soft actuator. Figure 4B shows the structure of the designed soft actuator for emulating the agonist-antagonist muscle pair. Two Ni-Ti SMA fibers, representing agonist and antagonist muscle fibers, are embedded on opposite sides of the polydimethylsiloxane (PDMS) matrix. Application of electricity causes the fibers to shrink in length owing to the structural deformation accompanied by the phase transition in the fiber. In particular, compressive and tensile strains are induced in the sides with a higher and lower voltage, respectively, resulting in the bending of the actuator toward the direction in which the higher voltage is applied. Figure 4C shows a schematic of the actuator when V_{ES}' and V_{IS}' are applied on each Ni-Ti SMA fiber. The amplitude of V_{ES}' is larger than that of V_{IS}', leading to the bending of the PDMS matrix to the V_{ES}' side. Owing to the inverse relationship between V_{ES}' and V_{IS}', one side contracts and the other side relaxes. Figure 4D shows the simulated strain distribution diagram of the three-dimensional (3D) modeled actuator subjected to the same pressure allocation as the Ni-Ti SMA fiber–embedded PDMS actuator. The tensile strain induced by the contraction on the other side is prominently reduced, indicating that the actuator exhibits a synergistic bending motion, as expected. Figure 4E shows the bending angle (BA) of the actuator as a function of $V_{ES}' - V_{IS}'$ (denoted as $\Delta V'$) with the fitted line. The direction of bending depends on whether $V_{ES}' - V_{IS}'$ is positive or negative, suggesting that the designed system can produce bidirectional motion.

Last, the operational performance of the ARIS is evaluated to demonstrate the efficacy of the designed system (see movie S1). Figure 4F shows real-time observations of the changes in $V_{ES}' - V_{IS}'$ ($\Delta V'$) with V_{pre}, along with photographs of the actuator in each condition. First, as consecutive input pulses of +2 V are applied to the V_{pre} terminal, $\Delta V'$ gradually increases and approaches +5 V. Consequently, the soft actuator bends, from BA of 0° (state 1) to 14° (state 2). Next, pulses of −2 V are applied until the actuator gradually returns to its original position (state 3). Second, pulses of the same amplitude (+2 V) are applied to the V_{pre} terminal. $\Delta V'$ approaches +9 V, causing bending of the actuator from states 3 to 4 with the corresponding BA of 34°. Subsequently, consecutive pulses of −2 V are applied to ensure that the actuator returns to the original position (state 5). The difference in BA between states 2 and 4 is 20°. In this case, the range of muscle movement is controlled by applying different numbers of V_{pre} pulses. Subsequently, successive V_{pre} pulses of +3 V are applied, and the actuator transforms from states 5 to 6. In this case, the BA value (34°) is the same as that of state 4; however, the time required for the change from the original position is different (12.6 s from states 3 to 4 and 6.4 s from states 5 to 6). This scenario is one in which the speed of muscle movement is controlled through the V_{pre} pulse amplitude. The same trend can be observed in the opposite direction. When continuous input pulses of −3 V are applied to the V_{pre} terminal, $\Delta V'$ rapidly approaches −10 V, resulting in the change in the actuator from states 7 to 8 with a corresponding BA of −36°. Subsequently, input pulses of +3 V are applied to promptly return the actuator to the original position, followed by the application of the input pulses of −2 V to the V_{pre} terminal. $\Delta V'$ gradually approaches −10 V, causing the soft actuator to bend from states 9 to 11. The time required for the actuator bending to the same level under different input voltages was 6.24 s from states 7 to 8 (at V_{pre} of −3 V) and 14.65 s from states 9 to 11 (at V_{pre} of −2 V). These results confirm that analog control of the actuator can be realized by changing the number and amplitude of the input pulses, and in particular, the operating speed can be controlled by the input voltage amplitude. Note that the pulse-driven characteristic of our system enables the lower energy consumption compared to the all-CMOS–based circuit (table S1).

DISCUSSION

We developed a motor control system that can mimic human reciprocal inhibition by using ESC/ISC, voltage/current amplifiers, and a soft actuator to demonstrate human muscle movement. The O-I hybrid GPSi was used as a gate dielectric for both the AS and load transistor in the ESC and ISC: GPSi annealed at 230°C served as the retentive dielectric for the AS, whereas GPSi annealed at 180°C served as a typical dielectric for the load transistor. By connecting the AS and load transistor in series, we designed the ESC and ISC connected to the Ni-Ti SMA fibers embedded in the PDMS matrix. By exploiting the inverse relationship of the output voltages of the ESC and ISC, reciprocal inhibition could be successfully emulated. In other words, relaxation on one side could be realized to accommodate the contraction of the other side of the actuator. The speed, range, and direction of the actuator bending could be precisely controlled via the preset input voltages. The proposed implementation of AS-integrated ESC and ISC as logic gates can facilitate follow-up research on the AS-integrated logic circuit–based complex system and can promote the application of these devices in bioinspired soft robots and prostheses.

MATERIALS AND METHODS

Device fabrication

To fabricate the load transistor and AS, a 30-nm-thick ITO layer was deposited onto a glass substrate via radio frequency magnetron sputtering. Subsequently, the ITO layer was patterned by conventional photolithography (AZ 5214E), followed by chemical etching with 35 volume % (vol %) hydrochloric acid diluted in distilled water. Next, a 30-nm-thick IGZO layer was deposited onto the ITO layer via radio frequency magnetron sputtering, followed by sintering at 300°C for 2 hours. The sintered IGZO layer was patterned by conventional photolithography, followed by chemical etching with 3 vol % LCE-12 (Cyantek Co.) diluted in distilled water. Moreover, 6 weight % GPSi sol, dissolved in ethanol, was spin-coated onto the IGZO layer at 3000 rpm for 60 s, followed by annealing at 180°C for 1 hour (load transistor) and 230°C for 2 hours (AS) in the ambient condition. In addition, a 40-nm-thick Al gate electrode was evaporated through a shadow mask onto the gate dielectric layer. To fabricate the soft actuator, a 100 mm by 20 mm by 6 mm (length × width × height) mold for PDMS was prepared using a 3D printer (Prusa MK3S). Four polytetrafluoroethylene (PTFE) tubes (diameter = 0.92 mm; Misumi, TUBF26-10) were placed through the holes of the mold to provide paths for the Ni-Ti SMA fibers (diameter = 0.5 mm; DYNALLOY Inc.). Subsequently, the uncured PDMS (SYLGARD 184) was poured into the mold, coupled with the PTFE tubes, and placed in vacuum for 30 min to extract the bubbles remaining in the PDMS. The PDMS was cured at 80°C, followed by the removal of the mold. The Ni-Ti SMA fiber was threaded through the PTFE tube and connected to the electrodes in the body of the actuator.

Measurements

EIS measurements were obtained using a VersaSTAT4 potentiostat (AMETEK). FTIR spectroscopy was performed using a Spectrum Two FTIR spectrometer (PerkinElmer) in the attenuated total reflection mode. XPS measurements were obtained using the VG ESCALAB 250 (Thermo Fisher Scientific) instrument, equipped with a monochromatic Al-Kα radiation source ($h\nu$ = 1486.8 eV). Raman spectroscopy was conducted using an alpha300 R (WITec) device with an excitation wavelength of 632.8 nm. The electrical properties of the transistors were measured using a Keithley 4200A-SCS instrument. Bending simulation was conducted via the SimScale Multiphysics simulation software using the 3D modeled soft actuator with the same pressure allocation as that of the Ni-Ti SMA–embedded PDMS soft actuator. The BA was measured through the ImageJ PhotoBend plugin using the recorded video at the side of the actuator.

SUPPLEMENTARY MATERIALS

Supplementary material for this article is available at https://science.org/doi/10.1126/sciadv.abo3326

REFERENCES AND NOTES

1. S. T. Keene, C. Lubrano, S. Kazemzadeh, A. Melianas, Y. Tuchman, G. Polino, P. Scognamiglio, L. Cinà, A. Salleo, Y. van de Burgt, F. Santoro, A biohybrid synapse with neurotransmitter-mediated plasticity. *Nat. Mater.* **19**, 969–973 (2020).

2. H. Kim, J. Choi, K. K. Kim, P. Won, S. Hong, S. H. Ko, Biomimetic chameleon soft robot with artificial crypsis and disruptive coloration skin. *Nat. Commun.* **12**, 4658 (2021).
3. D. G. Roe, S. Kim, Y. Y. Choi, H. Woo, M. S. Kang, Y. J. Song, J.-H. Ahn, Y. Lee, J. H. Cho, Biologically plausible artificial synaptic array: Replicating Ebbinghaus' memory curve with selective attention. *Adv. Mater.* **33**, 2007782 (2021).
4. S. Seo, S.-H. Jo, S. Kim, J. Shim, S. Oh, J.-H. Kim, K. Heo, J.-W. Choi, C. Choi, S. Oh, D. Kuzum, H. S. P. Wong, J.-H. Park, Artificial optic-neural synapse for colored and color-mixed pattern recognition. *Nat. Commun.* **9**, 5106 (2018).
5. Y. van de Burgt, E. Lubberman, E. J. Fuller, S. T. Keene, G. C. Faria, S. Agarwal, M. J. Marinella, A. Alec Talin, A. Salleo, A non-volatile organic electrochemical device as a low-voltage artificial synapse for neuromorphic computing. *Nat. Mater.* **16**, 414–418 (2017).
6. C. Wan, P. Cai, X. Guo, M. Wang, N. Matsuhisa, L. Yang, Z. Lv, Y. Luo, X. J. Loh, X. Chen, An artificial sensory neuron with visual-haptic fusion. *Nat. Commun.* **11**, 4602 (2020).
7. H. Wan, Y. Cao, L.-W. Lo, J. Zhao, N. Sepúlveda, C. Wang, Flexible carbon nanotube synaptic transistor for neurological electronic skin applications. *ACS Nano* **14**, 10402–10412 (2020).
8. Y. Wang, Y. Gong, S. Huang, X. Xing, Z. Lv, J. Wang, J.-Q. Yang, G. Zhang, Y. Zhou, S.-T. Han, Memristor-based biomimetic compound eye for real-time collision detection. *Nat. Commun.* **12**, 5979 (2021).
9. X. Yang, T. Zhou, T. J. Zwang, G. Hong, Y. Zhao, R. D. Viveros, T.-M. Fu, T. Gao, C. M. Lieber, Bioinspired neuron-like electronics. *Nat. Mater.* **18**, 510–517 (2019).
10. C. Zhang, W. B. Ye, K. Zhou, H.-Y. Chen, J.-Q. Yang, G. Ding, X. Chen, Y. Zhou, L. Zhou, F. Li, S.-T. Han, Bioinspired artificial sensory nerve based on nafion memristor. *Adv. Funct. Mater.* **29**, 1808783 (2019).
11. C. Laschi, B. Mazzolai, M. Cianchetti, Soft robotics: Technologies and systems pushing the boundaries of robot abilities. *Sci. Robot.* **1**, eaah3690 (2016).
12. J. Liang, Y. Wu, J. K. Yim, H. Chen, Z. Miao, H. Liu, Y. Liu, Y. Liu, D. Wang, W. Qiu, Z. Shao, M. Zhang, X. Wang, J. Zhong, L. Lin, Electrostatic footpads enable agile insect-scale soft robots with trajectory control. *Sci. Robot.* **6**, eabe7906 (2021).
13. H. Lu, Z. Zou, X. Wu, C. Shi, Y. Liu, J. Xiao, Biomimetic prosthetic hand enabled by liquid crystal elastomer tendons. *Micromachines* **12**, 736 (2021).
14. X. Wang, B. Yang, D. Tan, Q. Li, B. Song, Z.-S. Wu, A. del Campo, M. Kappl, Z. Wang, S. N. Gorb, S. Liu, L. Xue, Bioinspired footed soft robot with unidirectional all-terrain mobility. *Mater. Today* **35**, 42–49 (2020).
15. Y. Wu, J. K. Yim, J. Liang, Z. Shao, M. Qi, J. Zhong, Z. Luo, X. Yan, M. Zhang, X. Wang, R. S. Fearing, R. J. Full, L. Lin, Insect-scale fast moving and ultrarobust soft robot. *Sci. Robot.* **4**, eaax1594 (2019).
16. M. Cianchetti, C. Laschi, A. Menciassi, P. Dario, Biomedical applications of soft robotics. *Nat. Rev. Mater.* **3**, 143–153 (2018).
17. D. Rus, M. T. Tolley, Design, fabrication and control of soft robots. *Nature* **521**, 467–475 (2015).
18. Z. Shen, X. Zhu, C. Majidi, G. Gu, Cutaneous ionogel mechanoreceptors for soft machines, physiological sensing, and amputee prostheses. *Adv. Mater.* **33**, 2102069 (2021).
19. Y. Lee, T.-W. Lee, Organic synapses for neuromorphic electronics: From brain-inspired computing to sensorimotor nervetronics. *Acc. Chem. Res.* **52**, 964–974 (2019).
20. P. Li, H. P. Anwar Ali, W. Cheng, J. Yang, B. C. K. Tee, Bioinspired prosthetic interfaces. *Adv. Mater. Technol* **5**, 1900856 (2020).
21. Y. Chen, G. Gao, J. Zhao, H. Zhang, J. Yu, X. Yang, Q. Zhang, W. Zhang, S. Xu, J. Sun, Y. Meng, Q. Sun, Piezotronic graphene artificial sensory synapse. *Adv. Funct. Mater.* **29**, 1900959 (2019).
22. M. Karbalaei Akbari, S. Zhuiykov, A bioinspired optoelectronically engineered artificial neurorobotics device with sensorimotor functionalities. *Nat. Commun.* **10**, 3873 (2019).
23. S. Kim, D. G. Roe, Y. Y. Choi, H. Woo, J. Park, J. I. Lee, Y. Choi, S. B. Jo, M. S. Kang, Y. J. Song, S. Jeong, J. H. Cho, Artificial stimulus-response system capable of conscious response. *Sci. Adv.* **7**, eabe3996 (2021).
24. Y. Kim, A. Chortos, W. Xu, Y. Liu, J. Y. Oh, D. Son, J. Kang, A. M. Foudeh, C. Zhu, Y. Lee, S. Niu, J. Liu, R. Pfattner, Z. Bao, T.-W. Lee, A bioinspired flexible organic artificial afferent nerve. *Science* **360**, 998–1003 (2018).
25. Y. Lee, J. Y. Oh, W. Xu, O. Kim, T. R. Kim, J. Kang, Y. Kim, D. Son, J. B.-H. Tok, M. J. Park, Z. Bao, T.-W. Lee, Stretchable organic optoelectronic sensorimotor synapse. *Sci. Adv.* **4**, eaat7387 (2018).
26. D.-G. Seo, Y. Lee, G.-T. Go, M. Pei, S. Jung, Y. H. Jeong, W. Lee, H.-L. Park, S.-W. Kim, H. Yang, C. Yang, T.-W. Lee, Versatile neuromorphic electronics by modulating synaptic decay of single organic synaptic transistor: From artificial neural networks to neuro-prosthetics. *Nano Energy* **65**, 104035 (2019).
27. H. Shim, K. Sim, F. Ershad, P. Yang, A. Thukral, Z. Rao, H.-J. Kim, Y. Liu, X. Wang, G. Gu, L. Gao, X. Wang, Y. Chai, C. Yu, Stretchable elastic synaptic transistors for neurologically integrated soft engineering systems. *Sci. Adv.* **5**, eaax4961 (2019).
28. H. Wei, R. Shi, L. Sun, H. Yu, J. Gong, C. Liu, Z. Xu, Y. Ni, J. Xu, W. Xu, Mimicking efferent nerves using a graphdiyne-based artificial synapse with multiple ion diffusion dynamics. *Nat. Commun.* **12**, 1068 (2021).
29. Y. Zhu, C. Wu, Z. Xu, Y. Liu, H. Hu, T. Guo, T. W. Kim, Y. Chai, F. Li, Light-emitting memristors for optoelectronic artificial efferent nerve. *Nano Lett.* **21**, 6087–6094 (2021).
30. Y. Choi, S. Oh, C. Qian, J.-H. Park, J. Cho, Vertical organic synapse expandable to 3D crossbar array. *Nat. Commun.* **11**, 4595 (2020).
31. Y. Liu, J. Zhong, E. Li, H. Yang, X. Wang, D. Lai, H. Chem, T. Guo, Self-powered artificial synapses actuated by triboelectric nanogenerator. *Nano Energy* **60**, 377–384 (2019).
32. X. Yang, J. Yu, J. Zhao, Y. Chen, G. Gao, Y. Wang, Q. Sun, Z. Wang, Mechanoplastic tribotronic floating-gate neuromorphic transistor. *Adv. Funct. Mater.* **30**, 2002506 (2020).
33. Y. H. Liu, L. Q. Zhu, P. Feng, Y. Shi, Q. Wan, Freestanding artificial synapses based on laterally proton-coupled transistors on chitosan membranes. *Adv. Mater.* **27**, 5599–5604 (2015).
34. Z. Sun, E. Ambrosi, A. Bricalli, D. Ielmini, Logic computing with stateful neural networks of resistive switches. *Adv. Mater.* **30**, 1802554 (2018).
35. Q. Liu, Y. Liu, J. Li, C. Lau, F. Wu, A. Zhang, Z. Li, M. Chen, H. Fu, J. Draper, X. Cao, C. Zhou, Fully printed all-solid-state organic flexible artificial synapse for neuromorphic computing. *ACS Appl. Mater. Interfaces* **11**, 16749–16757 (2019).
36. G. Indiveri, B. Linares-Barranco, T. Hamilton, A. Schaik, R. Cummings, T. Delbruck, S. Liu, P. Dudek, P. Häfliger, S. Renaud, J. Schemmel, G. Cauwenberghs, J. Arthur, K. Hynna, F. Folowosele, S. Saighi, T. Serrno-Gotarredona, J. Wijekoon, Y. Wang, K. Boahen, Neuromophic silicon neuron circuits. *Front. Neurosci.* **5**, 73 (2011).
37. I. Vujaklija, D. Farina, O. Aszmann, New developments in prosthetic arm systems. *Orthop. Res. Rev.* Volume **8**, 31–39 (2016).
38. C. Aymard, L. Chia, R. Katz, C. Lafitte, A. Pénicaud, Reciprocal inhibition between wrist flexors and extensors in man: A new set of interneurones? *J. Physiol.* **487**, 221–235 (1995).
39. C. Crone, Reciprocal inhibition in man. *Dan. Med. Bull.* **40**, 571–581 (1993).
40. M. L. Latash, 6 - Control with muscle activations, in *Fundamentals of Motor Control* (Academic, ed. 1, 2012), pp. 93–111.
41. H.-j. Kwon, H. Ye, Y. Baek, J. Hong, R. Wang, Y. Choi, I. Lee, C. E. Park, S. Nam, J. Kim, S. H. Kim, Printable ultra-flexible fluorinated organic-inorganic nanohybrid sol-gel derived gate dielectrics for highly stable organic thin-film transistors and other practical applications. *Adv. Funct. Mater.* **31**, 2009539 (2021).
42. O. Larsson, E. Said, M. Berggren, X. Crispin, Insulator polarization mechanisms in polyelectrolyte-gated organic field-effect transistors. *Adv. Funct. Mater.* **19**, 3334–3341 (2009).
43. B.-A. Mei, O. Munteshari, J. Lau, B. Dunn, L. Pilon, Physical interpretations of nyquist plots for EDLC electrodes and devices. *J. Phys. Chem. C* **122**, 194–206 (2018).
44. D. Kannaiyan, S. T. Kochuveedu, Y. H. Jang, Y. J. Jang, J. Y. Lee, J. Lee, J. Lee, J. Kim, D. H. Kim, Enhanced photophysical properties of nanopatterned titania nanodots/nanowires upon hybridization with silica via block copolymer templated sol-gel process. *Polymers* **2**, 490–504 (2010).
45. G.-W. Hong, S. Ramesh, J.-H. Kim, H.-J. Kim, H.-S. Lee, Synthesis and properties of cellulose-functionalized POSS-SiO_2/TiO_2 hybrid composites. *J. Nanosci. Nanotechnol.* **15**, 8048–8054 (2015).
46. L. Hongyan, X. Hou, L. Chai, X. Cui, Y. Wang, T. Deng, Efficient and green catalytic degradation of high crosslinked rigid PU foam and recovery value-added products via selective cleavage of C–O and C–N bonds. *Polym. Degrad. Stab.* **181**, 109262–102020 (2020).
47. M. Rodošek, M. Mihelčič, M. Čolović, E. Šest, M. Šobak, I. Jerman, A. K. Surca, Tailored crosslinking process and protective efficiency of epoxy coatings containing glycidyl-POSS. *Polymers* **12**, 591 (2020).
48. A. Fina, D. Tabuani, F. Carniato, A. Frache, E. Boccaleri, G. Camino, Polyhedral oligomeric silsesquioxanes (POSS) thermal degradation. *Thermochim. Acta* **440**, 36–42 (2006).
49. M. Hernández-Escolano, X. Ramis, A. Jiménez-Morales, M. Juan-Díaz, J. Suay, Study of the thermal degradation of bioactive sol-gel coatings for the optimization of its curing process. *J. Therm. Anal. Calorim.* **107**, 499–508 (2012).
50. B. A. Howell, W. Sun, Thermal degradation of esters/ethers derived from tartaric acid. *J. Therm. Anal. Calorim.* **122**, 1167–1175 (2015).
51. J. Macan, I. Brnardić, S. Orlić, H. Ivanković, M. Ivanković, Thermal degradation of epoxy–silica organic–inorganic hybrid materials. *Polym. Degrad. Stab.* **91**, 122–127 (2006).
52. B. Wang, M. Shi, J. Ding, Z. Huang, Polyhedral oligomeric silsesquioxane (POSS)-modified phenolic resin: Synthesis and anti-oxidation properties. *e-Polym.* **21**, 316–326 (2021).
53. J. Choi, J. Yoon, M. J. Kim, K. Pak, C. Lee, H. Lee, K. Jeong, K. Ihm, S. Yoo, B. J. Cho, H. Lee, S. G. Im, Spontaneous generation of a molecular thin hydrophobic skin layer on a sub-20 nm, high-k polymer dielectric for extremely stable organic thin-film transistor operation. *ACS Appl. Mater. Interfaces* **11**, 29113–29123 (2019).
54. C. Frenkel, M. Lefebvre, J.-D. Legat, D. Bol, A 0.086-mm2 12.7-pJ/SOP 64k-synapse 256-neuron online-learning digital spiking neuromorphic processor in 28-nm CMOS. *IEEE Trans. Biomed. Circuits Syst.* **13**, 145–158 (2019).

Acknowledgments

Funding: This work was supported by the Creative Materials Discovery Program through the National Research Foundation of Korea (NRF) funded by the Ministry of Science and ICT grant NRF-2019M3D1A1078299 (to J.H.C.), Materials and Components Technology Development Program (20006537, Development of High Performance Insulation Materials for Flexible OLED Display TFT) funded by the Ministry of Trade, Industry, and Energy (MOTIE, Korea) (to J.H.C.), and a Korea Medical Device Development Fund grant funded by the Korean government (the Ministry of Science and ICT) (project number: KMDF202012B02-02 to J.H.C.). **Author contributions:** Conceptualization: Seonkwon Kim, Seongchan Kim, D.G.R., and J.H.C. Methodology: Seongchan Kim, D.H.H., D.G.R., Y.J.C., and M.L.L. Investigation: Seonkwon Kim, U.J.K., and S.H.K. Visualization: Seonkwon Kim and Seongchan Kim. Funding acquisition: M.J.K. and J.H.C. Project administration: J.H.C. Supervision: J.K., S.H.K., and J.H.C. Writing (original draft): Seonkwon Kim. Writing (review and editing): Seonkwon Kim, M.J.K., and J.H.C. **Competing interests:** The authors declare that they have no competing interests. **Data and materials availability:** All data needed to evaluate the conclusions in the paper are present in the paper and/or the Supplementary Materials.

Submitted 28 January 2022
Accepted 11 August 2022
Published 28 September 2022
10.1126/sciadv.abo3326